



OPEN Longitudinal seismic responses of large diameter shield tunnel crossing liquefied bank slope

Xiaoxiong Li^{1,2}✉, Haiyang Zhuang^{1,4}, Bin Ruan³, Kai Zhao¹✉ & Guoxing Chen¹

The lateral spread of the fluvial terraces due to liquefaction can cause tremendous physical damage to the underground structure. This paper designs a liquefaction slippage site and discusses the feasibility of the generalized response displacement method for investigating the seismic response of shield tunnels in liquefaction slippage areas. According to the actual shield tunnel project across the lower reaches of the Yangtze River, a 4.8-km large-scale liquefaction site and a refined beam-spring shield tunnel model based on the generalized response displacement method are established, respectively. Further, the seismic response of the shield tunnel is evaluated. The numerical results show that for the focus area: (1) The generalized response displacement method can consider the influences of topographic effects and site liquefaction slippage on the longitudinal seismic response of the shield tunnel. (2) The site slippage of bank slope is harmful to the safety of the large-diameter tunnel structure, as it may cause a large longitudinal opening width at the ring intersegment as well as sudden changes in section tension and pressure. (3) The bending moment variation curve and the acceleration amplification factor curve along the tunnel axis are consistent with the site topography, and the curves show obvious abrupt changes in the liquefied slippage areas.

Keywords Shield tunnel, Generalized response displacement method, Liquefied slippage, Opening width at ring intersegment, Seismic response

With rapidly developing of urban rail transit and the coordinated development of riverside and coastal urban agglomerations, the shield tunnel project is developing rapidly^{1,2}. The shield tunnel crosses the lower reaches of the Yangtze River, which has a gently slope and a considerable amount of newly deposited cohesionless soils exist on both sides of the valley³. Under strong seismic waves, it is very easy to cause earthquake disasters, such as the liquefied slippage. The liquefaction of the stratum will cause the change of the load balance relationship and increase the stress in the structure Section^{4,5}. The liquefaction slippage of the site may increase the opening width and aggravate the concrete damage at the joint. ‘Standard for Seismic Design of Underground Structures (GB/T 51336-2018) states shield tunnels should not cross strata that may experience liquefaction. However, when bypassing is not possible, the adverse effects of liquefaction on the structural safety and stability should be analyzed, and seismic and damping measures should be taken. Therefore, the potential impact of site liquefaction slip on the structural safety cannot be ignored.

The shield tunnel is an ultra-long linear structure that takes up a lot of space and generally lasts several kilometers. Accordingly, the tunnel will inevitably cross different soil layers with large differences in stiffness^{6,7}. Considerable researches have shown that near the soil interface, the structure’s seismic response increases significantly^{6,8,9}. Hence, more attention should be paid on the longitudinal seismic performance of the shield tunnel. The shield tunnel is assembled by segments, ring bolts, and longitudinal bolts, and such flexible connection construction is conducive to reducing seismic forces. However, it leads to several problems such as susceptibility to damage at tunnel joints and poor integrity. This was confirmed by the post-earthquake disaster investigation of the shield tunnel^{10–13}. Therefore, the flexible connection of bolts needs to be considered when investigating the longitudinal seismic response characteristics.

Unlike superstructures, underground structures are completely buried in the soil. The structure is not limited by the inertial forces, but rather by the soil surrounding it, and the surrounding soil is responsible for more

¹Institute of Geotechnical Engineering, Nanjing Tech University, Nanjing 210009, People’s Republic of China.

²College of Civil and Architecture Engineering, Chuzhou University, Chuzhou 239000, People’s Republic of China.

³National Center of Technology Innovation for Digital Construction, School of Civil and Hydraulic Engineering, Huazhong University of Science and Technology, Wuhan 430074, People’s Republic of China. ⁴School of Civil Engineering and Architecture, East China Jiaotong University, Nanchang 330013, People’s Republic of China.

✉email: lixx20201105@163.com; zhaokai@njtech.edu.cn

than 95% of the seismic response^{14–17}. The theory of emphasizing the deformation of the foundation free field is widely used in the seismic design of underground structures^{18–20}. 'Code for Seismic Design of Urban Rail Transit Structures (GB50909-2014) adopt the response displacement method. The tunnel structure and foundation soil are simplified as continuous beams and springs, respectively. However, this method assumes that the sinusoidal distribution of the stratum is inconsistent with the spatial displacement distribution of the non-uniform site. The calculated results based on accurate vibration state and stratum spring stiffness are almost consistent with the results of complex dynamic analysis^{21,22}. From this point of view, Chen et al.²³ proposed the generalized response displacement method. The method considers the nonlinear characteristics of the soil layer in the inhomogeneous site under seismic waves, and investigates the longitudinal seismic response characteristics.

The quasi-static method is generally used to calculate the longitudinal seismic response of shield tunnel. Therefore, in this paper, the quasi-static method-generalized response displacement method proposed by the research group is used to study the longitudinal seismic response of shield tunnel crossing the liquefied slip zone. This method takes the deformation of the free field layer as the seismic equivalent load, and loads the displacement time history of the free field nodes into the beam-spring model. However, the nonlinearity of the site soil and the kilometer-scale (4.8 km) lateral deformation limit the computability of the numerical simulation of such sites. This article focuses on the complexity of the terrain and the particularity of the strata of the wide valley site in the lower reaches of the Yangtze River, and combines the geological profile of the actual engineering site to establish a refined model of the wide valley site in the lower reaches of the Yangtze River. The established viscoelastic plastic constitutive model for large deformation of sand liquefaction and the ALE method have been adopted to solve the difficulty of simulating slip large deformation at this type of site. Subsequently, a 4.8 km refined beam-spring shield tunnel model was established to study the longitudinal seismic responses of large-diameter shield tunnel crossing liquefied bank slope. The research results could improve the understanding of the earthquake damage mechanism of tunnels crossing the liquefied slippage area.

Engineering overview

The lower reaches of the Yangtze River entrance to the sea is selected. The site has wide multi-stage terraces and flood plain on both sides, and the slope of the valley is generally $1^\circ \sim 2^\circ$, which is significantly smoother than that of the conventional valley. Due to the special sedimentary environment, the terrace is characterised by a typical binary stratified rhythmic structure²⁴. Local changes in hydrodynamic conditions during deposition form the lenticular bodies in the sand layer. Since large quantities of sand that is carried downstream and deposited here, a very loose and thick layer of sand is formed each year of which the sand is the typical Nanjing sand, which is more liquefiable²⁵. The site is susceptible to liquefaction slippage under strong seismic waves.

The topographic relief of the project varies greatly along the north–south direction. According to the standard penetration test of soil layers in the geotechnical investigation report for the Sutong GIL pipe gallery engineering project, the average value of 20 m liquefaction index I_{LE} of a total of 15 hole numbers in ①₁ and ②₂ soil layers on the south bank is 26.1, and the liquefaction degree of soil layers is severe (According to 'Code for Seismic Design of Buildings (GB50011-2016) $0 < I_{LE} \leq 6$ slight, $6 < I_{LE} \leq 18$ moderate, $18 < I_{LE}$ severe). The top of both ends of the tunnel with an outer diameter of 11.6 m is 8 m–10 m away from the ground surface. The tunnel crosses ②₂ layers. Figure 1 shows the north–south section along the tunnel. Table 1 shows the parameters of soil layer. $G_0 = \rho \cdot v_s^2$, where ρ and v_s are the density and shear wave velocity of the soil layer, respectively.

Generalized response displacement method numerical modeling

Free-field site model

The true size of geometry model was provided by the geotechnical investigation report of the site as a CAD drawing, as shown in Fig. 1. A finite element model of the referred wide river valley of Yangtze River is established at the scale of several kilometers, fully considering the fluvial terrace features and non-uniform spatial distribution, as presented in Fig. 2. The numbers in Fig. 2 represent different soil layers, with specific

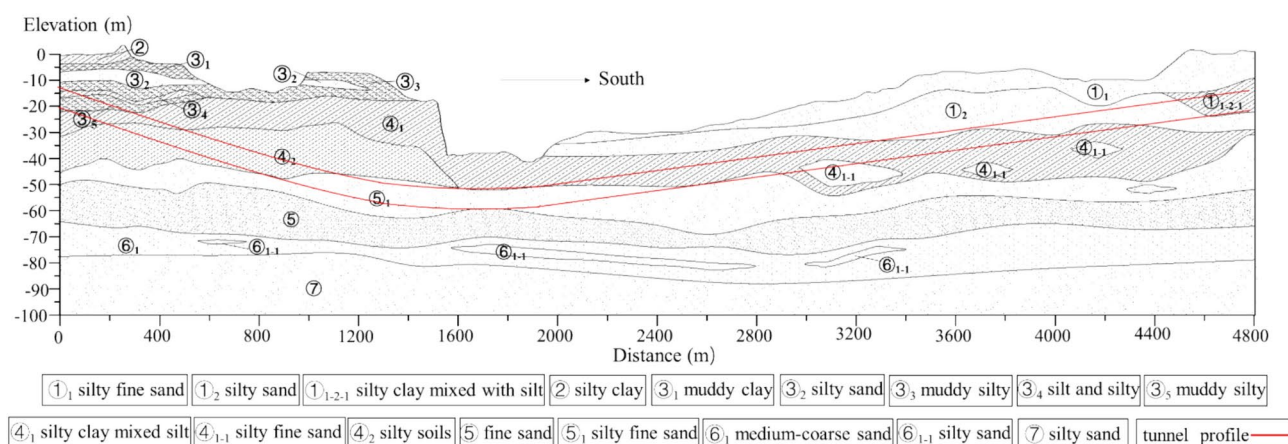


Fig. 1. The site cross-section.

Soil name	Maximum initial shear modulus G_0 (MPa)	Weight (kN/m ³)	Internal friction angle ϕ (°)	Young's modulus (MPa)	Poisson's ratio ν
① ₁ silty fine sand	33	19.6	34.2	4.5	0.37
① ₂ silty sand	63	19.3	28.0	4.5	0.34
① ₁₋₂₋₁ silty clay mixed with silt	47	18.3	33.9	7.8	0.34
② silty clay	109	18.9	24.7	2.3	0.37
③ ₁ muddy clay	18	18	21.3	1.5	0.39
③ ₂ silty sand	49	19.3	31.2	3.9	0.34
③ ₃ muddy silty	46	18.1	19.9	1.5	0.39
③ ₄ silt and silty	114	18.3	25.3	6.5	0.34
③ ₅ muddy silty	46	18.0	23.6	2.5	0.39
④ ₁ silty clay mixed silt	59	18.1	24.5	5.2	0.34
④ ₁₋₁ silty fine sand	172	19.1	35.2	9.2	0.29
④ ₂ silty soils	123	18.2	28.6	10.5	0.32
⑤ fine sand	216	19.8	33.6	40.9	0.26
⑤ ₁ silty fine sand	201	19.6	34.0	22.9	0.29
⑥ ₁ medium-coarse sand	220	20.2	35.2	48.0	0.27
⑥ ₁₋₁ silty sand	250	19.3	38.2	37.5	0.25
⑦ silty sand	304	20	31.6	26.0	0.34

Table 1. Physical and mechanical parameters of the soils.

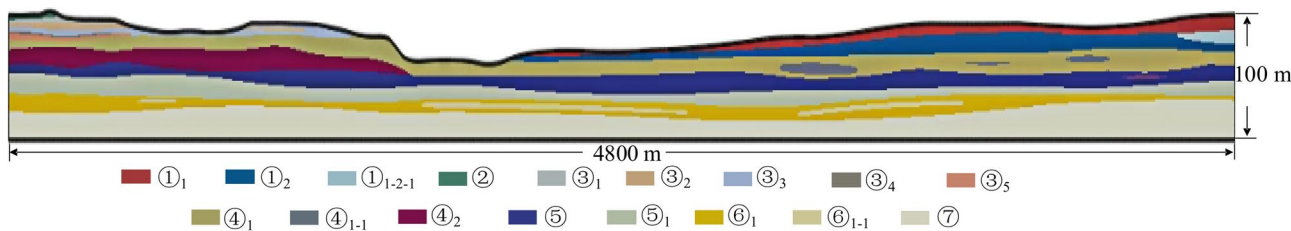


Fig. 2. Free-field site model.

layer names consistent with those in Fig. 1. Additionally, the seismic response of several kilometers of site must consider the traveling wave effect. The nodes within 50 m of the bottom of the free field are a set and the wave speed is 1000 m/s. The travelling wave effect is simulated by the phase difference of the set distance/wave speed conversion at each node of the foundation. In the model, the underground water depth is located at the ground surface, while the overlying water is not considered.

Under the cyclic loading, the shear modulus should degenerate with the number of cyclic loading and the dynamic deformation of soil should show the unidirectional accumulation property, which could not be simulated by the Mohr–Coulomb model or (modified) Cam-clay model. Due to the above problem, the visco-elastoplastic memorial nested yield surface model is employed to simulate the liquefaction behavior of the sandy soil in the lower reaches of Yangtze River, which is originally proposed by Elgamal and Yang, and recently improved by Zhuang et al.²⁶ In particular, the mixed hardening modulus field theory combining the isotropic hardening and dynamic hardening is adopted, as presented in Fig. 3. In the stress–strain relationship expression of the constitutive model, Rayleigh damping is introduced to account for the viscosity effect of the soil. Using dynamic triaxial test to verify the feasibility of this dynamic constitutive model²⁷. The calculation dynamic parameters of liquefiable sand ①₁ are determined, shown in Table 2. The constitutive calculation parameters of the other soil layer are derived from the parameters in Table 1²⁷. The established viscoelastic plastic constitutive model for large deformation of sand liquefaction and the ALE method have been adopted to solve the difficulty of simulating slip large deformation at this type of site.

Within an effective stress site response framework, the present manuscript adopts a loosely coupled approach that predicts excess pore water pressure by adopting relationships used in combination with constitutive models that address total stress. Based on the volumetric compatibility condition of the soil skeleton and pore water in the dynamic Biot theory, the change in excess pore water pressure ΔP is directly related to the increment in volumetric strain $\Delta \epsilon_v$ for undrained conditions,

$$\Delta P = K \Delta \epsilon_v \tag{1}$$

Note that the bulk modulus, K , plays an important role in determining the magnitude of the cyclic loading impact on the generation of excess pore water pressure. The excess pore water pressure is thereby predicted

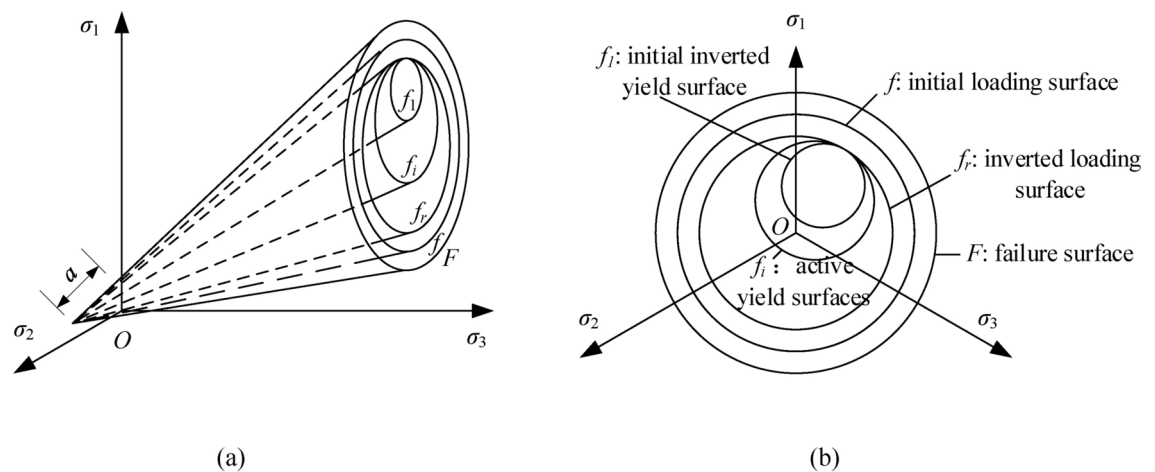


Fig. 3. Yield surfaces in the principal stress space and the deviatoric plane. (a) The yield surfaces in stress space; (b) The yield surfaces in deviatoric plane.

Parameters	Value	Parameters	Value
Reference shear modulus	$G_0 = 49 \text{ MPa}$	Contraction	$c_1 = 0.15, c_2 = 0.5$
Reference mean pressure	$p_0 = 100 \text{ kPa}$	Hardening	$e_1 = 0.8, e_2 = 2.8$
Pressure dependence exponent	$n_p = 0.5$	Dilation	$d_1 = 0.3, d_2 = 100$
Friction angle	$\phi = 32^\circ$	Locking strain	$\gamma_1 = 0.01, \gamma_2 = 0$
Phase transformation angle	$\phi_{pt} = 28^\circ$	Locking release pressure	$p_y = 0.5 \text{ kPa}$
Residual strength pressure	$a = 5 \text{ kPa}$	Slip strain	$\gamma_{sl} = 0.01$

Table 2. Dynamic calculation parameters of liquefiable sand.

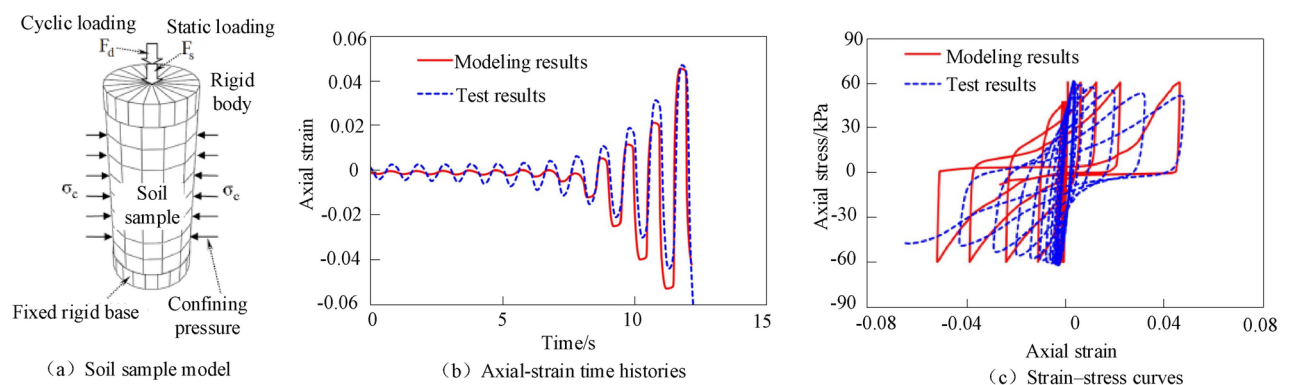


Fig. 4. Predicted results of the finite element method compared with the test results.

at each time step with respect to the plastic irreversible volumetric strain, which is calculated by the visco-elastoplastic memorial nested yield surface model.

Furthermore, we make the undrained condition assumption of the fluvial terraces at the lower reaches of Yangtze River during earthquakes as tradition, because of 1) the low soil permeability of river sediments of concern and 2) high rate of loading caused by strong earthquake shaking. Under the undrained condition, no relative movement of the pore fluid and also re-consolidation are permitted, i.e., $k = 0$ ^{28,29}.

To verified the constitutive model of the liquefiable soil model and the constitutive parameters in Table 2, A 3-D numerical model has then developed to model the dynamic responses of a sand sample tested in a dynamic triaxial machine³⁰. Then, the predicted axial-strain time histories and the strain-stress curves are compared with the test results, as shown in Fig. 4, which shows that the constitutive parameters are reasonable.

The initial geostatic stress conditions of the surrounding soil will have a major impact on its dynamic characteristics. In previous analysis methods, the static analysis step and the dynamic analysis step were analyzed separately, and then the calculation results of two steps are added together, these methods can not consider

the influence of the initial geostatic stress on the dynamic properties of the soil. To solve this problem, the static-dynamic coupling finite element analysis model was developed by Zhuang et al.³¹. In this model, before performing dynamic analysis step, the static stress state is calculated and the dynamic shear modulus of the soils was updated based on the static confining stress, the static and dynamic analysis steps are coupled together.

The model analysis process includes static analysis and dynamic analysis: 1) Prior to performing seismic response analysis, the static analysis step is needed to impose the initial stress in the model. The bottom boundary is set a fixed constraint, and the lateral boundaries on both sides are only fixed at the horizontal direction. 2) In the process of seismic response analysis, the lateral boundaries are released at the horizontal direction from the static analysis step. Thus, the lateral boundaries are horizontally free and vertically constrained. In addition, horizontally loaded reaction force (RF), which is obtained by static analysis. As shown in Fig. 5.

The model boundary handling is important for the seismic response of the site. Due to the complicated geological condition of the site, it is very difficult by using the analytic boundary treatment method to weaken the reflective wave from the different directions induced by the non-homogeneous soil layers. To solve this problem, the lateral boundaries of the finite element model in this study was set to be wider than the main wide river valley to weaken the reflective wave from the lateral boundaries by the additional lateral soils. In addition, Chen et al.³² used the same boundary treatment as in this paper, and the feasibility of the numerical simulation was verified by model test.

Numerical model of soil-tunnels system

Using the generalized response displacement method proposed by Chen et al.²³, a refined shield tunnel beam-spring model is established, as shown in Fig. 6. The tunnel segment is simplified as a 3D linear beam element (B31). The beam elements are disconnected from each other to simulate the ring segment joints. The seismic response is coupled by the longitudinal, transverse, and vertical⁷. Therefore, the connection between beam elements needs to consider the seismic response in different directions. In consideration of this, the axial spring K_a , rotational spring K_θ , and shear spring K_s are used to connect each beam element in the model. The beam element in the software cannot present the elliptical deformation of the cross-section. Therefore, this deformation of structure is not taken into account in the article.

It is shown in Tables 3 and 4 for the basic mechanical parameters of the segments and the connecting bolts. There are 22 longitudinal bolts at each circumferential seam of the tunnel. The longitudinal deformation of the tunnel under seismic wave is composed of tensile and compressive deformation. When the tunnel is in tension, the connecting bolts between the segment rings provide tensile force, and the sum of the stiffnesses of the connecting bolts is the joint's axial tensile stiffness. When the tunnel is compressed, the pressure is only borne by the segment ring, the segment ring concrete provides the axial compressive stiffness. Therefore, the joint bolts exhibit different nonlinear characteristics in tension and compression. In consideration of the tunnel bending deformation, the tunnel cross-section consists of compressive and tensile zones. The tensile force is supported by the connecting bolt; the compressive zone is supported by the segment ring, and the concrete of the segment ring is always in the elastic state²³. Table 5 gives the nonlinear bolts and torsion springs. The beam element is a circular ring with an inner and outer diameter of 11.8 m and 10.6 m respectively, and the length is 2 m. The tunnel length is 4800 m, the length of each segment is 2 m, and there are 2400 beam elements. A total of 7197 connection springs is set between the beam elements and 9600 subgrade springs-dampers are built around the tunnel. However, the initial stress of the bolt is neglect in this study in that it has weaker effect on the seismic responses under the larger soil deformation.

The extraction and loading of free-field displacements and the building of the beam-spring model are more cumbersome in the generalized response displacement method. Therefore, this paper uses ABAQUS (Abaqus 6.14, <https://www.3ds.com/products-services/simulia/products/abaqus/>) and Python (Python 3.9, <https://www.python.org/downloads/release/python-390/>) joint modeling. Firstly, the free field model is established using ABAQUS (Abaqus 6.14, <https://www.3ds.com/products-services/simulia/products/abaqus/>) software. The soil nodes at the buried depth of the tunnel in the free field are set as a special node set, and the nodes in this set are renumbered longitudinally along the buried depth of the tunnel. Subsequently, the free-field model seismic response calculation is carried out, and Python (Python 3.9, <https://www.python.org/downloads/release/python-390/>)

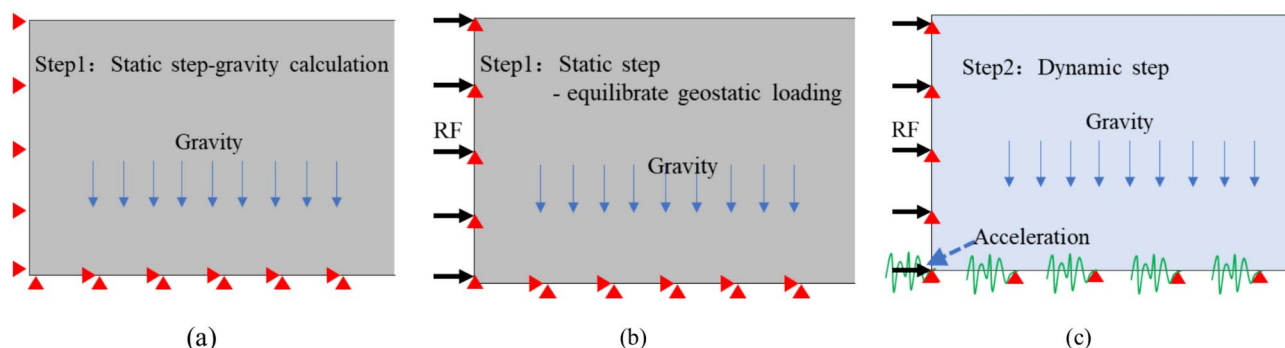


Fig. 5. Transformation settings. (a) Static analysis step; (b) Equilibrate geostatic loading; (c) Dynamic analysis step-input acceleration.

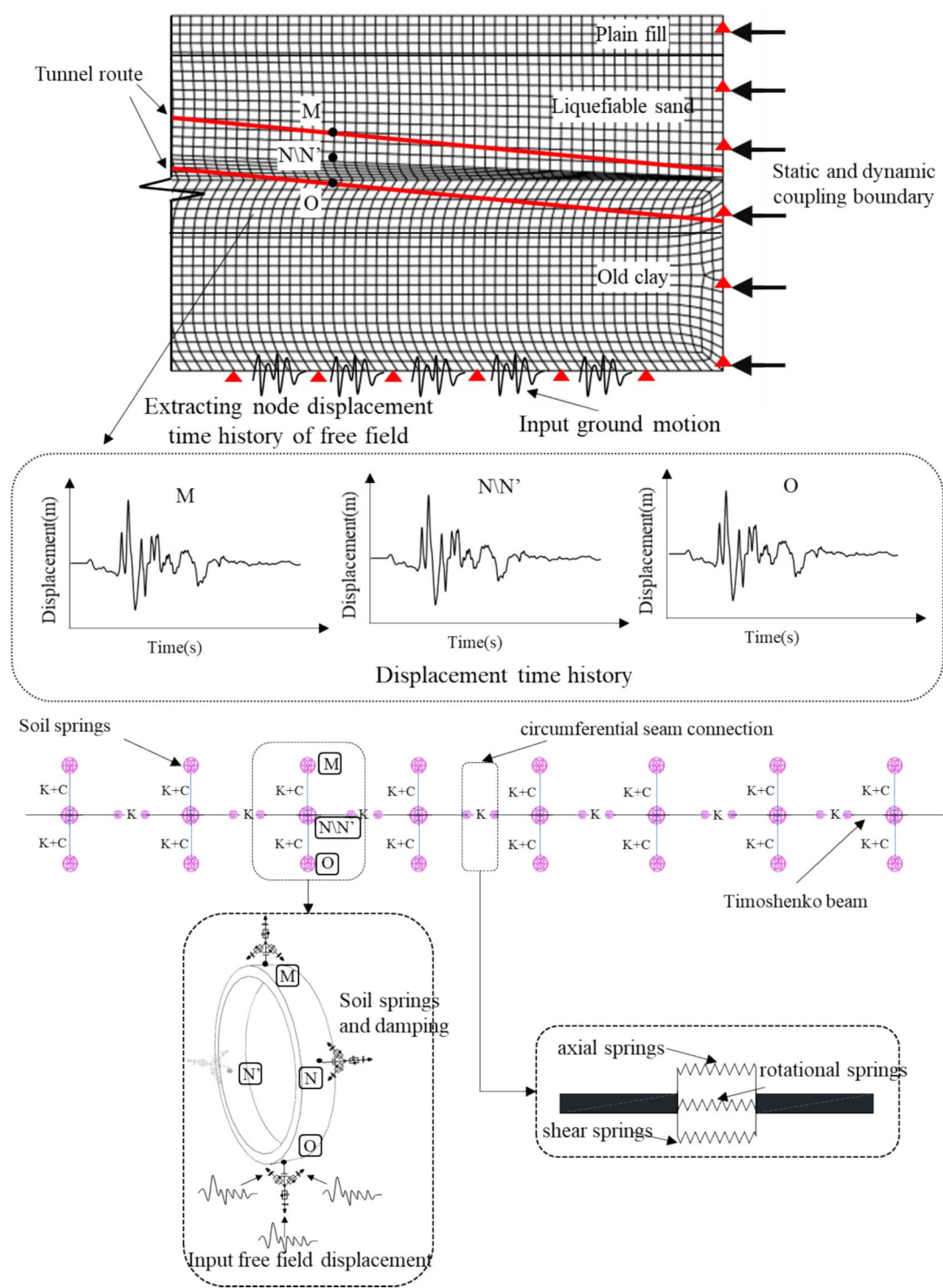


Fig. 6. Schematic diagram of the generalized response displacement method.

Concrete mark	Outside diameter D/m	Inside diameter d/m	Segment length l_s/m	Elastic modulus E_c/GPa	Poisson's ratio
C60	11.6	10.5	2	36	0.2

Table 3. Parameters of the concrete segment.

Diameters d_0 /mm	Length l_0 /mm	Elastic modulus E_s /GPa	Tensional rigidity /kN/m	Shear stresses /GPa	Elastic-plastic stiffness ratio α
40	648	206	432	1.09	0.01

Table 4. Ring joint bolt parameters.

Compression stiffness K_c (kN)	Initial tension stiffness K_{u1} (kN)	Post-yield tension stiffness K_{u2} (kN)	Tensile ultimate force N_m (kN)	Tensile yield force N_y (kN)	Yield Deformation /Ultimate Deformation $\delta y/\delta m$
3.44E11	9.5E9	9.5E7	2.29E4	1.93E4	2.0/39.9
Post-yield bending stiffness $K_{\theta 2}$ (kN-m/rad)	Initial bending Stiffness $K_{\theta 1}$ (kN-m/rad)	Ultimate Moment M_m (kN-m)	Yield moment M_y (kN-m)	Ultimate rotational angle θ_m (rad)	Yield rotational angle θ_y (rad)
4.38E9	3.89E11	8.74E4	6.90E4	4.4E-3	1.78E-4

Table 5. Nonlinear spring parameters of pipe-ring joint.

on-390/) is used to extract quickly the displacement time history of each node in the set. By calculating the spatial coordinates of each beam element of the model, the establishment of the beam element is completed in combination with the math library of Python (Python 3.9, <https://www.python.org/downloads/release/python-390/>). The reference point is established around the beam element, and the spring is used to connect the adjacent beam element endpoint, the reference point and the beam element (soil springs) respectively. Based on the xldr library in Python (Python 3.9, <https://www.python.org/downloads/release/python-390/>), the free field node displacement time history stored in the excel file is easily loaded into the reference point around the beam, and the seismic response calculation of the shield tunnel model is completed. In addition, during the construction of shield tunnel, synchronous grouting or secondary grouting should be carried out in a certain range of soil layer outside the segment³³. The surrounding rock grouting reinforcement reduces the relative dislocation displacements between the structure and the surrounding rock during earthquakes. Therefore, the model in this paper does not consider the separation between structure and soil.

The difference of initial stresses in the soil around the tunnel is large, so the subgrade spring stiffness at different locations in the same section needs to be calculated separately. The horizontal longitudinal k_x and transverse k_y subgrade spring stiffness coefficients are computed as below³⁴.

$$k_x = k_y = \frac{16\pi G_s(1 - \nu_m)}{3 - 4\nu_m} \frac{d}{L} \quad (2)$$

The vertical subgrade spring stiffness coefficient is calculated using the following formula³⁵.

$$k_z = \frac{2\pi G_s}{1 - \nu_m} \frac{d}{L} \quad (3)$$

where G_s is the soil shear modulus, ν_m is the soil Poisson's ratio, d is the diameter of the shield tunnel, L is the wavelength. According to 'Code for Seismic Design of Urban Rail Transit Structures (GB50909-2014)' G_s denotes the shear modulus of foundation soil corresponding to the maximum strain amplitude of the earthquake vibration. Based on the results of free field calculations to extract the maximum strain amplitude. Combined with the results of the $G/G_{\max} \sim \gamma$ tests of the newly deposited soils in the lower reaches of the Yangtze River entrance to the sea³⁶, the non-liquefied soil layer G_s is determined. For liquefied soil layers, the attenuation function of shear modulus with cumulative deformation amplitude of unidirectional flow under mega-deformation after initial liquefaction of saturated fine sand is given by³.

$$\frac{G_s}{G_0} = 12.07\gamma_{SA}^{-1.065} \times 10^{-3} \quad (4)$$

where, G_0 initial maximum shear modulus, γ_{SA} cumulative strain amplitude of unidirectional flow after liquefaction of saturated fine sand. The G_s of the liquefied soil is then determined.

In order to effectively simulate the tunnel-soil interaction, dampers are set around the tunnel beam element. The damping coefficient in different directions also differs. The horizontal longitudinal C_x , horizontal transverse C_y and vertical C_z subgrade spring damping coefficients are computed as below³⁶.

$$C_x = \rho V_s \pi d \quad (5)$$

$$C_y = C_z = \rho V_s d + \rho V_{La} d \quad (6)$$

where V_s is the shear wave velocity, V_{La} is the Lysmer wave velocity, and the calculation formula is as follows.

$$V_{La} = \frac{3.4}{\pi(1 - \nu_m)} V_s \quad (7)$$

After liquefaction, the damping gradually decreases. According to the experimental results of Xu et al.³⁷ on the damping change of sandy soil after liquefaction, the damping coefficient of the liquefied layer is reduced.

Input motion selection

One of the most important issues on the seismic ground response analysis is the selection of input earthquake motion. It is preferable to select earthquake records observed in or near the target site. However, it is impossible due to the lack of recordings in this studied region as mentioned above. Also, the selected earthquake motions should cover a variety of characteristics (frequency content, duration, acceleration, and intensity) such as those representatives of earthquake mechanism along the lower reaches of Yangtze River. Therefore, representative earthquake records that have been often used in the earthquake resistant design are selected in this study. A set of three typical and commonly used ground motion records, Kobe motion, Shifangbajiao (SFBJ) motion and Mianzhuqingping (MZQP) motion are selected to be applied as input motions from the bedrock. The Kobe motion is selected mainly because significant damage occurred over a widespread area in Hyogo Prefecture and its vicinity during the 1995 Hyogoken-Nambu (Kobe) earthquake, as well as there are some slightly inclined site slips which induced severe damage to the coastal engineering³⁸. The recorded SFBJ motion and MZQP motion are of interest due to the reason that these two near-fault motions were recorded during the 2008 Wenchuan earthquake. Figure 7 illustrates the acceleration time histories and its corresponding Fourier spectra, respectively. These selected earthquake motions contain broad and rich frequency content in the North–South (NS) direction. Furthermore, the PGA (peak ground acceleration) /PGV (peak ground velocity) records at the Kobe-, SFBJ- and MZQP motions are 0.918, 0.508 and 1.220, respectively. Based on the classification criterion on the earthquake motions proposed by Tso et al.³⁹: 1) $\text{PGA}/\text{PGV} > 1.2$, high frequency motion; 2) $0.8 < \text{PGA}/\text{PGV} < 1.2$, medium-frequency motion; and 3) $\text{PGA}/\text{PGV} < 0.8$, low-frequency motion, these three selected earthquake motions cover a full range of the low-, medium- and high frequency motions accordingly.

Yu et al.⁴⁰ studied the earthquake damage of Longxi tunnel in Wenchuan earthquake in 2008, and combined with numerical analysis to prove that vertical ground motion can usually be ignored compared with longitudinal ground motion of tunnel. Furthermore, the Daikai station is the first well-documented case of a completely collapsed large underground structure subjected to ground motion. Most of the studies on the seismic damage of this subway station emphasize that the horizontal deformation of the soil layer is the main cause of shear damage to the structure. Horizontal ground shaking is the main cause, while the effect of vertical ground shaking is relatively limited^{41,42}. Finally, the recorded earthquake motions are scaled to 0.10 g, 0.15 g and 0.20 g by adjusting the original PGA and employed as horizontal input ground motions in the numerical analysis.

It should be emphasized that, since the width of this wide river valley site reaches to 4800 m, the seismic wave propagation at different locations may exhibit temporal asynchrony. Therefore, the traveling wave effect of the input ground motion must be considered. The traveling wave velocity adopted in the analysis is 1000 m/s. In the established numerical model, the nodes within 50 m at the model bottom form a set, and the traveling wave effect of seismic waves is simulated by inputting ground motions asynchronously among these different node sets.

The input of seismic wave in this paper only considers the phase difference in the propagation process, and does not consider the difference of amplitude. The reason for this simplification is that: 1) seismic waves propagate in bedrock with lower energy loss, faster wave velocity, more stable propagation, and the waveform change is small; 2) compared with the amplitude, the phase difference has a greater impact on the dynamic response and safety of the structure and site⁴³.

Method verification

Chen et al.^{21,23} verified the generalized response displacement method's accuracy by establishing a 3D FEA model of the surrounding rock tunnel, and applied it to the investigation of the longitudinal seismic response.

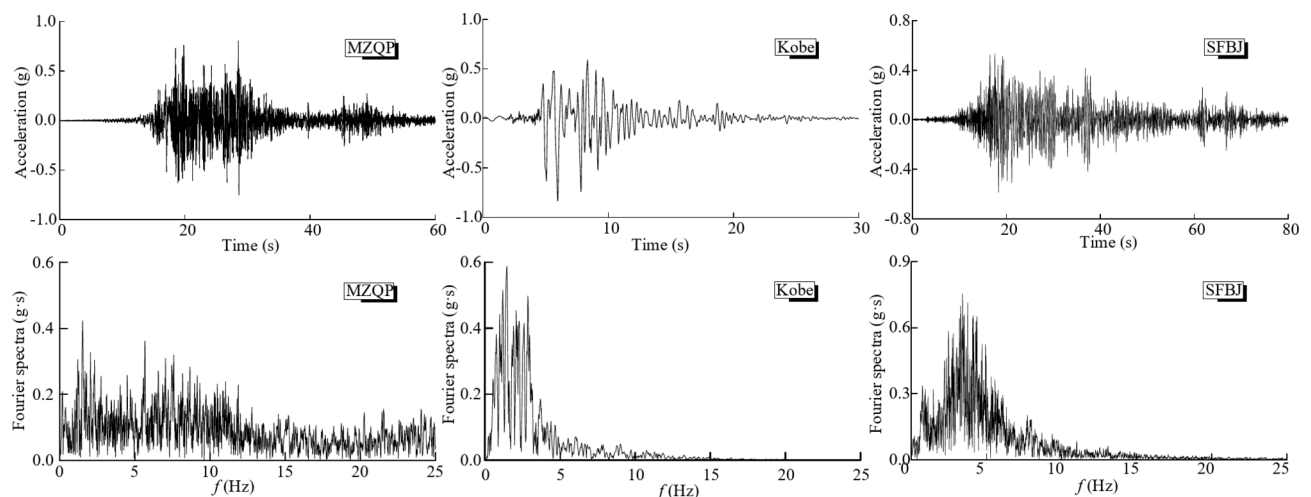


Fig. 7. Acceleration time-history and Fourier spectra at different earthquake events.

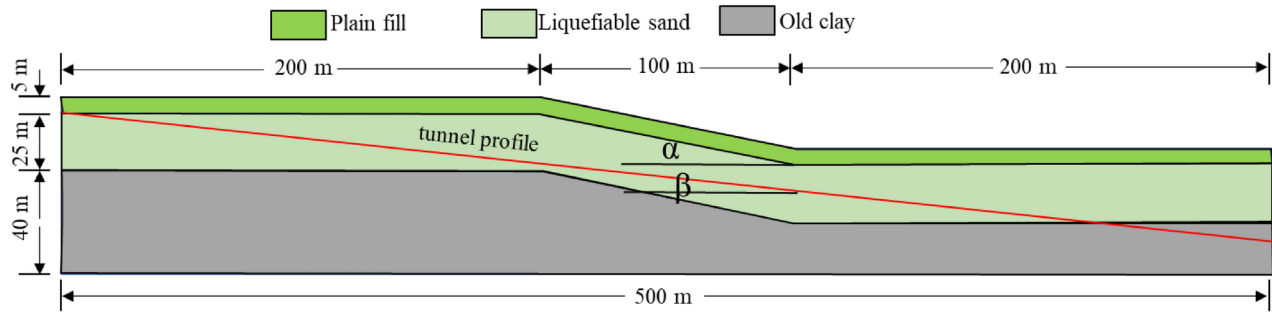


Fig. 8. Free-field site numerical model.

	ϕ Internal friction angle /°	Shear wave velocity /(m/s)	Poisson's ratio	Young's modulus /MPa	Weight /kN•m ³
Plain fill	28.0	150	0.34	2.5	18.3
Liquefiable sand	34.2	160	0.34	4.5	19.6
Old clay	38.2	330	0.25	37.5	20.2

Table 6. Physical parameters of soil layer.

Seismic waves	Slope α	Tunnel longitudinal slope β
Kobe-0.20 g	0°, 3°, 6°, 9°	4%

Table 7. Verification of the calculated conditions.

However, a further discussion is needed on the application of the generalized response displacement method on the longitudinal seismic response of shield tunnels crossing liquefied slippage zones. Therefore, a liquefied slippage site is designed to study the longitudinal seismic response. Further, the calculation results are checked against the findings of related scholars to verify the reliability of this method.

Verification scheme

During an earthquake, the liquefaction and plastic flow of the underlying soil causes tensile damage of the surface soil. The process of settlement, movement, rotation, decomposition, and flow of the damaged soil is known as liquefied slip phenomenon. There are two conditions for the formation of “liquefied slip”: 1) the sandy and silty soil foundations produces liquefaction under seismic action; 2) The surface is gentle slope or located near the free face. A liquefiable site was designed based on the lower reaches of the Yangtze River³, as shown in Fig. 8. The soil’s parameters are given in Table 6. The underground water level is set to be 1.0 m. The total length of the tunnel is 500 m, and there are 250 beam elements. A total of 747 connection springs are set between the beam elements, and 1000 dampers-subgrade springs are built around the tunnel. The parameters are shown in Table 3,4,5.

By analyzing the seismic response differences between under slope gradient change and the results from the literature, the rationality of the generalized response displacement method for the research of seismic response of shield tunnels in liquefied slippage areas is discussed. According to ‘Standard for Design of Shield Tunnel Engineering (GB/T51438-2021) the maximum gradient of the shield tunnel is not greater than 6%. Combined with above conditions, the changes of slope gradient α and tunnel longitudinal slope β in Fig. 8 are shown in Table 7. Current studies have shown that shield tunnels are less prone to structural damage under small intensity ground motions^{44,45}. Therefore, this paper focuses on the longitudinal nonlinear seismic response rule under 0.20 g.

Verification results

Distribution characteristics of site liquefaction slippage

The Fig. 9(a) shows the lateral slippage increases with the increase of the slope gradient. The 0° slope has no obvious liquefaction slippage, and the maximum slippage displacement of the 9° slope reaches 2.4 m. The number of sliding surfaces of the 6° and 9° slopes is significantly more than that of the 3° slopes. The sliding surface of the 3° slope shows a certain slope concave shape, but the 6° and 9° slopes are circular sliding surfaces. It can be found from the vertical displacement cloud map of the site Fig. 9 (b) that the starting point of ground surface uplift of 3° slope is at the slope surface, and the uplifts of the 6° and 9° slopes are located at the bottom. In addition, the 9° slope uplift is further away from the foot of the slope. The above rule confirms that the 6° and 9° slopes are circular sliding surfaces, and the sliding radius of the 9° slope is larger than 6° slope. Figure 10 shows that the liquefaction area of the 3° slope is significantly bigger than the other two working conditions. In accordance with

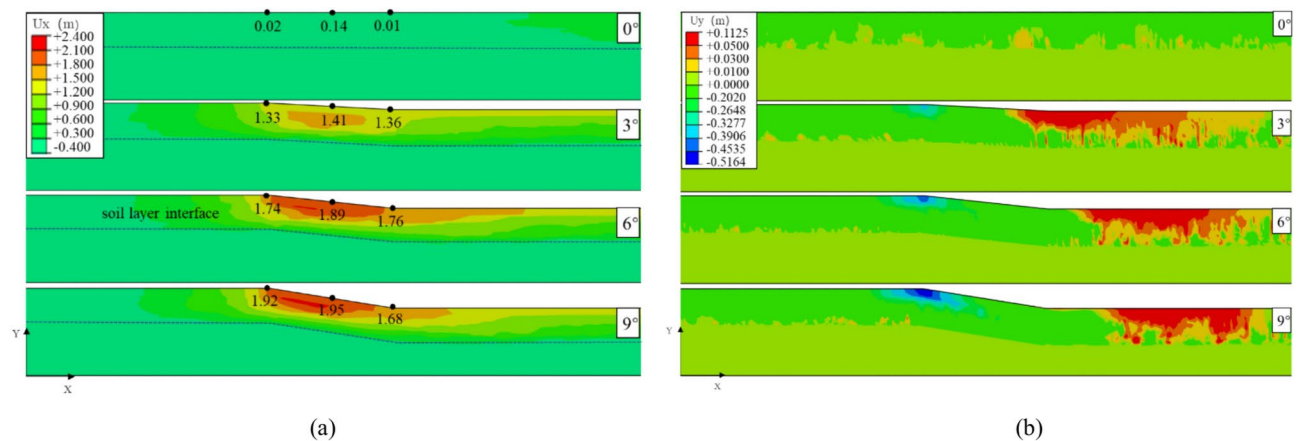


Fig. 9. Site liquefaction slippage after loading. (a) Horizontal displacement; (b) Vertical displacement.

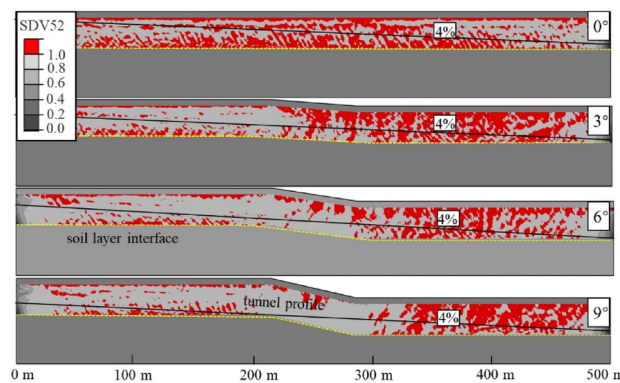


Fig. 10. Site liquefaction distribution.

the displacement cloud map, the lateral displacement induced by the liquefied slippage converts into circular shear deformation caused by the weakened shear strength of the soil layer when the slope gradient is large²⁷.

'General Rule for Performance-Based Seismic Design of Buildings (CECS160-2019) classifies the grade of ground lateral displacement induced by the liquefaction when the ground surface is gently inclined as slight (0–0.3 m), moderate (0.3 m–0.5 m), severe (0.5 m–1.0 m) and very severe (> 1.0 m). The lateral displacement under 0.2 g ground motion all exceeds 1.0 m, and the lateral displacement grade is very severe. From the top to the bottom of the slope, the overall trend of slope slippage displacement shows an increase followed by a decrease, which is consistent with the result of the centrifuge test by Taboada-Urtuzastegui et al.⁴⁶.

Figure 10 shows the distribution of site liquefaction, and the black curve represents the longitudinal axis of the structure. Figure indicates that sand has been liquefied (red zone) when SDV52 is greater than 1, where SDV52 is the dynamic pore pressure ratio. The liquefied area in the bottom of the slope is considerably bigger than in other locations. By considering Fig. 9, it is found that the soil layer at the bottom produces lateral slippage along the interface between non-liquefied and liquefied layers, and the slippage displacement along the depth upwards shows a stratification phenomenon. The shield tunnel in all working conditions only crosses the liquefaction zone.

Opening width at ring intersegment

The opening width under seismic wave is one of the important indicators for structural safety assessment of shield tunnels. The opening width is the maximum value of the difference between the displacement time histories of adjacent segments. As shown in Fig. 11, the value is the absolute value that the displacement time history at Point A minus that at Point B. Considering this, Fig. 12 shows the opening width curves along the tunnel longitudinal under different working conditions. The curve does not take into account that there is no opening within the 2 m width of a single segment, it is only the connection curve of the opening width.

Figure 12 shows that the amplitude of the opening width through the liquefied slippage zone varies significantly. It indicates that the liquefied slippage aggravated damage of the structure. The opening width at ring intersegment is divided into three sections: 0–100 m; 100–400 m; 400–500 m. The opening width under different working conditions from 0–100 m has little difference, and the overall change amplitude is small; the opening width varies greatly from 100–400 m, and the variability is large at different positions under the same working

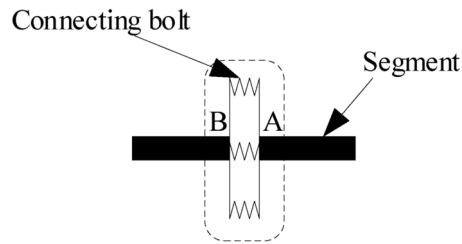


Fig. 11. Diagram of the opening width.

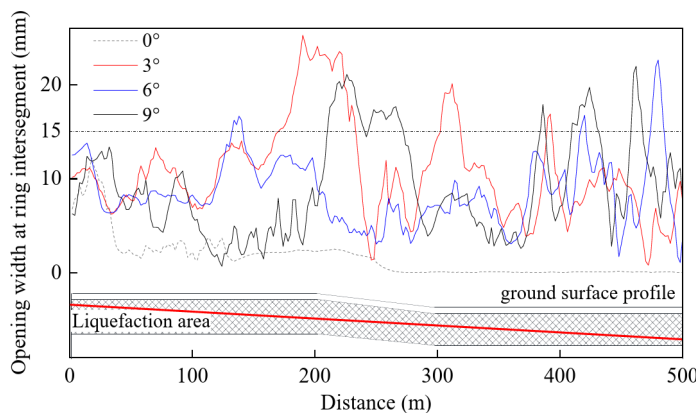


Fig. 12. Opening width of shield tunnel.

condition; the opening variation decreases under different working conditions from 400–500 m. The main reason for the dramatic change of the 100–400 m opening width is that 200–300 m is the main slippage zone, which has different soil slippage displacements along the longitudinal. Furthermore, the magnitude and variation of the opening width at the top of the 0–100 m is small than that at the bottom of the 400–500 m. Combined with Fig. 9(a), it can be seen that the above phenomenon is related to the soil slippage distribution pattern. The above phenomenon illustrates that using the generalized response displacement method, the longitudinal seismic response of the structure is mainly limited by the liquefied slip deformation. This is consistent with the conclusion that the surrounding soil deformation determines the seismic response of the structure^{14,16}.

The opening width of the tunnel crossing 0° slope is the same as other working conditions in the range of 0–30 m. However, with the increase of burial depth, the opening width at ring intersegment gradually decreases and is much smaller than other working conditions. Although the tunnel crosses the liquefaction zone of 0° slope, there is no significant slippage at the site. Therefore, the liquefaction of the site does not cause serious damage to the structure, and the liquefied slippage of the soil layer is the main cause. Furthermore, the slope slippage mode determines the variation pattern of the opening width.

Inner force

Figure 13 plotted the tensile force, compression curve, and bending moment maximum in the middle section of the longitudinal ring intersegment of the structure, respectively. Figure 13 (a)—13(b) show that the 0–300 m slope top and slope surface are mainly bearing axial tensile force, and the 300–500 m slope bottom is withstanding axial compression. The tensile force and compression curves are consistent with opening width curves in Fig. 12.

Figure 13(c) shows that the maximum value curve of the bending moment has a tendency to first increase and then decrease. The bending moment at the slope surface is larger than that at other locations, and there is a sudden change at the foot. The slope surface bending moment increase should be related to the ground motion amplification effect. The liquefaction degree of the soil at the foot of the slope is the most serious⁴⁷, which leads to a reduction of soil stiffness around the tunnel, thus causing the greater tunnel deformation at this location.

Acceleration response

Figure 14 shows the curve of the longitudinal acceleration amplification factors (AF) of the shield tunnel, which exhibits an overall trend of increasing and then decreasing. Where $AF = \text{peak acceleration of tunnel structure} / \text{peak bedrock acceleration (PBA)}$. The acceleration amplification factor at the top of the slope shows an approximately linear growth trend with the increase of slope gradient, but the difference is small under different working conditions at the bottom of the slope. Combined with Fig. 8, the rule is related to the burial depth of the tunnel. When the tunnel crosses a relatively gentle slope, the thicker the liquefied soil layer at the bottom of the tunnel, the more obvious the effect on seismic isolation. Furthermore, the amplification effect of the acceleration near the slope shoulder confirms the increasing trend of the tunnel bending moment at this location.

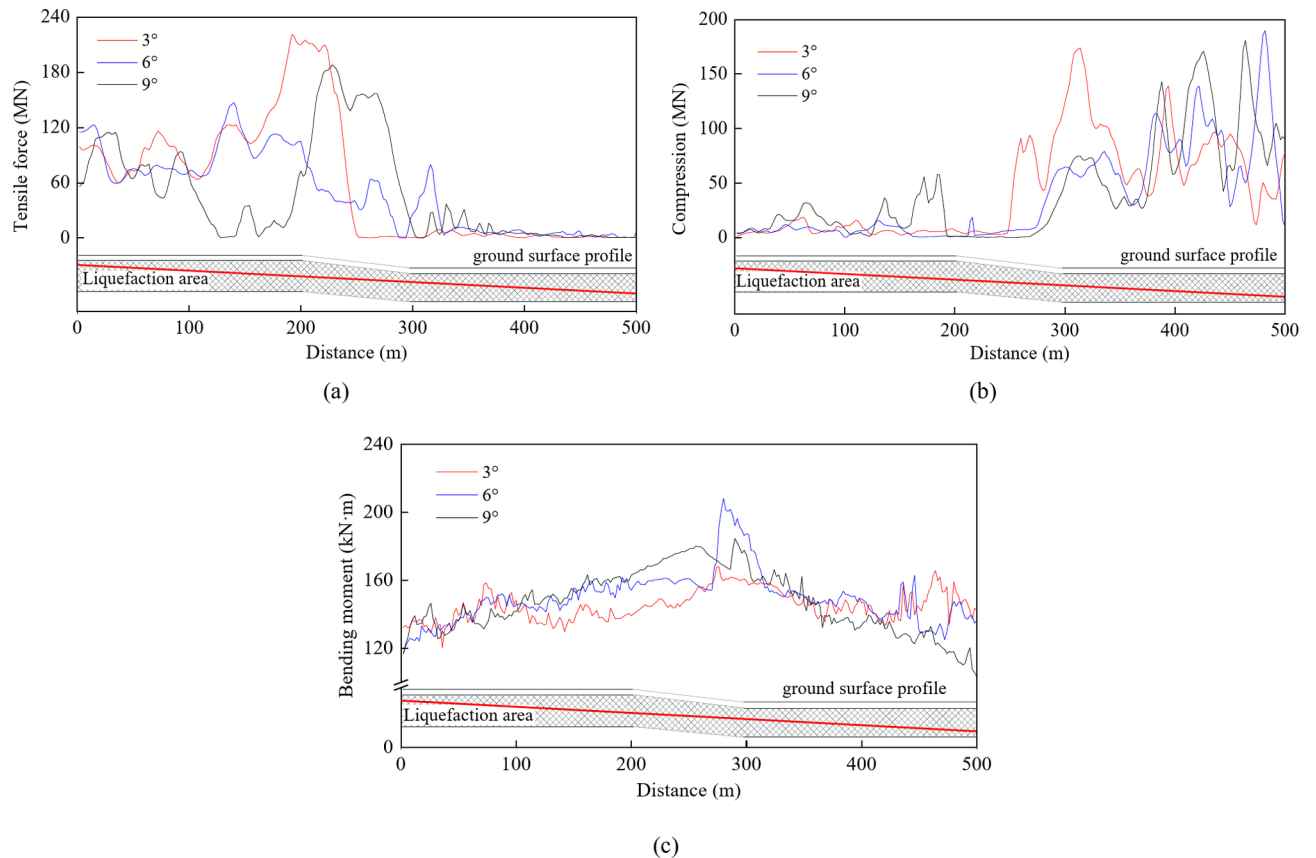


Fig. 13. Inner force response of shield tunnel. (a) Tensile force response; (b) Compression response; (c) Bending moment response.

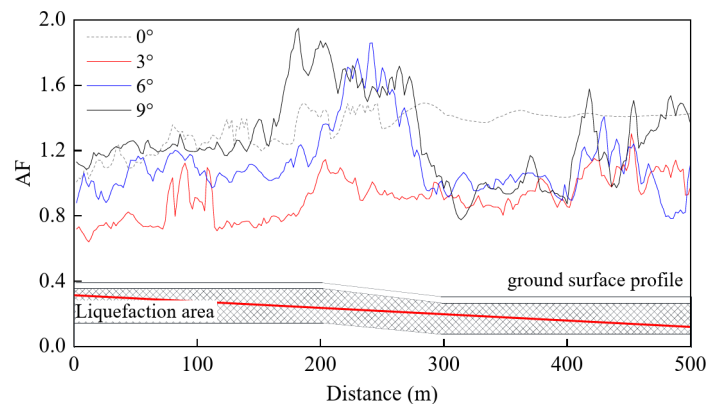


Fig. 14. Envelopes for AF of acceleration response.

Based on the generalized response displacement method, the shield tunnel deformation in the liquefied slippage areas is mainly constrained by the surrounding soil layer. This is consistent with the current research results on underground structural-stratum deformation^{14,16}. The severe liquefaction of the soil layer at the foot of the slope leads to a reduction of soil stiffness⁴⁷, and there is a peak of shield tunnel bending moment at the foot of the slope. Hence, the spring-damping adopted can simulate the tunnel-soil interaction. Figure 14 shows that the acceleration amplification at the shoulder of the slope, which is consistent with the seismic measured^{48,49}. Considering this, the generalized response displacement method can simulate the soil-structure interaction, which reproduces the influences of liquefied slippage deformation, topographic effects, and soil liquefaction on the longitudinal seismic response. Therefore, the generalized response displacement method is feasible for investigating the longitudinal nonlinear seismic response of shield tunnels in liquefied slippage areas.

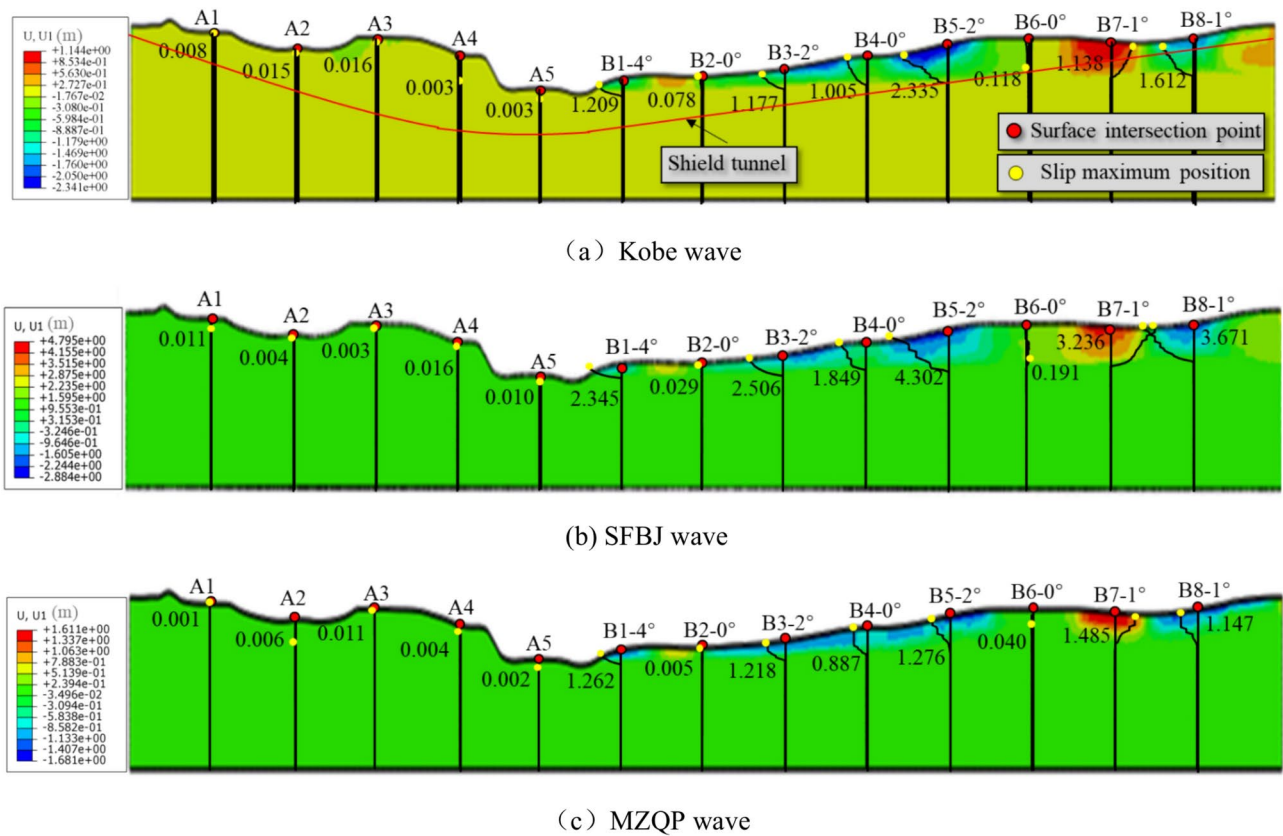


Fig. 15. Liquefaction slip relative displacement of sites under earthquake action (0.10 g).

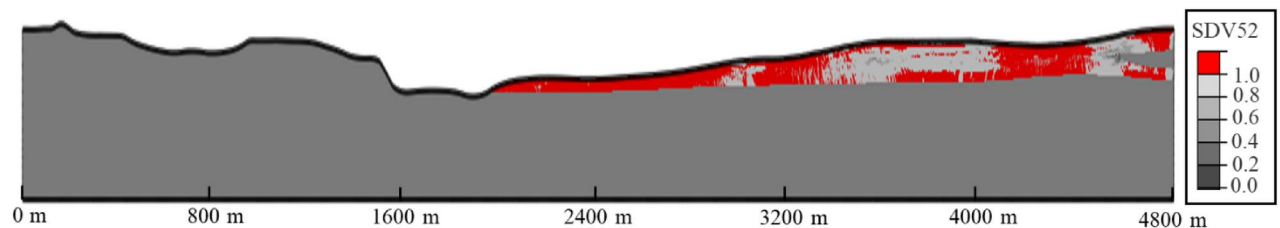


Fig. 16. Liquefaction distribution in case of the input Kobe (0.20 g).

Longitudinal seismic analysis of the shield tunnel

Site liquefaction slippage

The slippage pattern of the selected slightly inclined liquefiable sites, which is similar under different ground motion intensities. Therefore, this paper only plots the distribution of soil liquefaction areas and the relative lateral displacement curves on different paths between each node of the strata to the bottom of the foundation under 0.10 g. As shown in Fig. 15—Fig. 16, the red curve is the longitudinal axis of structure.

Figure 15—Fig. 16 show that the lateral displacement in zone B on the south bank is much larger than that in zone A. The maximum ground lateral displacement at the non-liquefied site in zone A is only centimeter level, but it reaches meter level in zone B. The lateral displacement in area B is caused by the large deformation of the shallow soil. Thus, the site produces a large lateral slippage under seismic wave action. The direction of the slip is consistent with the slope direction, and the larger slips occur at the surface location of the slope with a certain slope. In general, the lateral slippage is caused by the accumulation of lateral displacement of the liquefiable layer, which mainly occurs in the lower part of the liquefiable layer, and then slowly increase to the ground surface along the depth. It should be noted that the direction of the slope at point B7 is opposite to that at other points. Therefore, the lateral slippage direction of the ground surface at point B7 is also changed. The slope produces lateral shift towards the valley bottom between B7 and B8, and the soil will accumulate at the bottom. At the same position, the amplitude of ground lateral spreading was highest for the input SFBJ motion, intermediate for the input Kobe motion, and lowest for the input MZQP motion, as determined by the calculations. The initial stress state in the slope has a strong influence on the spatial distribution of liquefaction. The stress state at

the soil element is gradually transformed from a state of triaxial compression to a state of triaxial tension as the position changes from the slope crest to the slope toe. It is worth carrying out further study on the influence of initial stress state on the liquefaction behavior within the slope to verify and explain the above variation pattern. The influence law of the spectrum characteristics of the seismic wave needs to be further investigated. The shield tunnel crosses the liquefaction zone at 3500–4800 m, and the slippage zone at 3500 ~ 3720 m and 4010 ~ 4520 m. The slip patterns of the wide valley site under different types of ground motions are similar, and the seismic response of the underground structures is limited by the surrounding soil layers¹⁶. Therefore, the longitudinal seismic response of the shield tunnels under the action of Kobe seismic waves is only investigated.

Longitudinal seismic response of tunnel

Longitudinal opening width at ring intersegment

The longitudinal flexible connection of the bolts at the ring intersegment is susceptible to large opening width. To ensure the overall waterproofing of the structure, the maximum opening width should be smaller than the limit with 15 mm margin¹⁶. Figure 17 (a) plots the curve of the opening width. To comprehensively investigate the change rule of opening width, the failure value is defined as 1 when the opening width exceeds the 15 mm limit, otherwise, it is defined as 0. Figure 17 (b) gives the opening failure curve.

Figure 17 shows that the lateral liquefaction slippage of the site will result in a large opening width. The maximum value in the non-liquefaction area varies less with the increase of PBA, and all of them are less than 15 mm. However, in the liquefaction zone, it is found that the opening width increases sharply with the increase of PBA. When the PBA is 0.20 g, the maximum value reaches 119 mm. The opening width at ring intersegment will inevitably lead to the failure of connecting bolts, which will further aggravate the damage degree. Therefore, the liquefaction slippage of the site has an extremely adverse impact on the seismic safety.

The opening width at the ring intersegment varies extremely drastically in the liquefied slippage zone. The above phenomenon indicates that the vibration of the shield tunnel in the liquefied slippage zone has a complex interaction with the surrounding soil, and the maximum value of the opening width is not linearly increasing with the PBA. The maximum value position under different ground motion intensities is located near 4520 m. There are three peaks along the longitudinal, which are located at 3500 m, 4200 m, and 4520 m, respectively. Combined with Fig. 15– Fig. 16, It could be observed that the peak of the opening width are located at the interface between the slippage zone and the non-slippage zone, and 3500 m is also the transition interface of the liquefaction layer. In addition, the opening width less than the limit value locate near the valley bottom at 4350 m between B7 and B8. The above phenomenon further verifies that the seismic response of the shield tunnel is mainly restrained by the liquefied slippage deformation of the surrounding soil.

Inner force seismic response

Several earthquake damage of structure studies have shown that shield tunnels are prone to concrete damage under earthquake action¹². The efficiency of the transverse equivalent bending stiffness of shield tunnels is several to tens of times higher than that of longitudinal^{50,51}. The tunnels extend longitudinally over several kilometers and have to cross different soil layers, and the soft and hard uneven soil layers will further lead to more severe longitudinal deformation. Therefore, it is important to investigate the internal force distribution rule along the longitudinal. Figure 18 shows the seismic response of the tunnel inner forces.

Figure 18 (a) shows that the lateral liquefaction slippage under earthquake action will result in large axial tensile forces in the shield tunnel ring intersegment. The overall variation trend under different ground motion intensities is similar, and it increases with the increase of PBA. The longitudinal segments are connected by 22 grade 10.9 bolts, and the ultimate tensile force of the ring seams of the segments that can withstand is 27.6 MN. However, the axial tensile force of the tunnel section in the liquefied slippage area exceeds the limit value, and the maximum tensile force reaches 1160 MN when the PBA is 0.20 g. The large tensile force inevitably leads to tensile damage of the connecting bolts. Overall, the change trend of the tensile force along the longitudinal is consistent with the opening width, and the tensile force at the slippage interface has a sudden change.

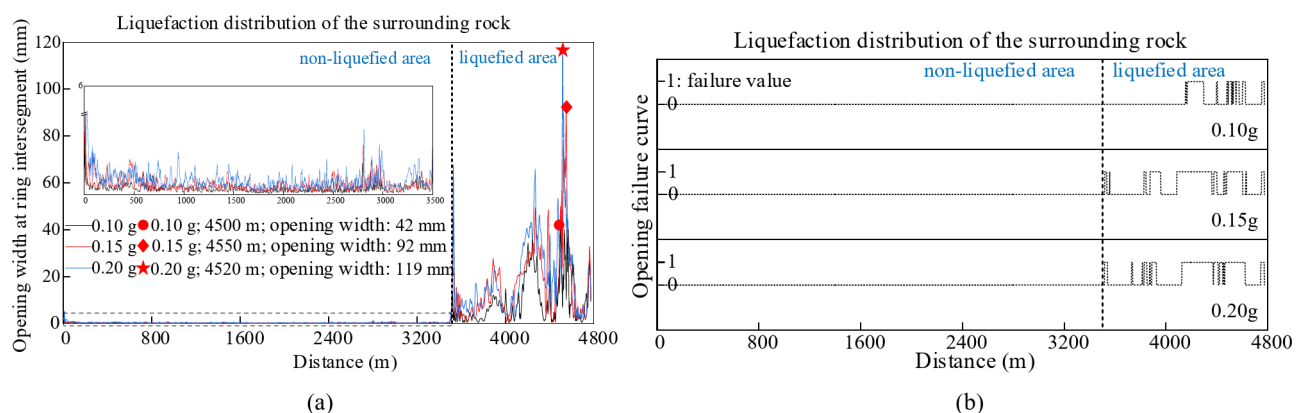


Fig. 17. The opening width along the tunnel longitudinal direction. (a) Opening width at ring intersegment; (b) Opening failure curve.

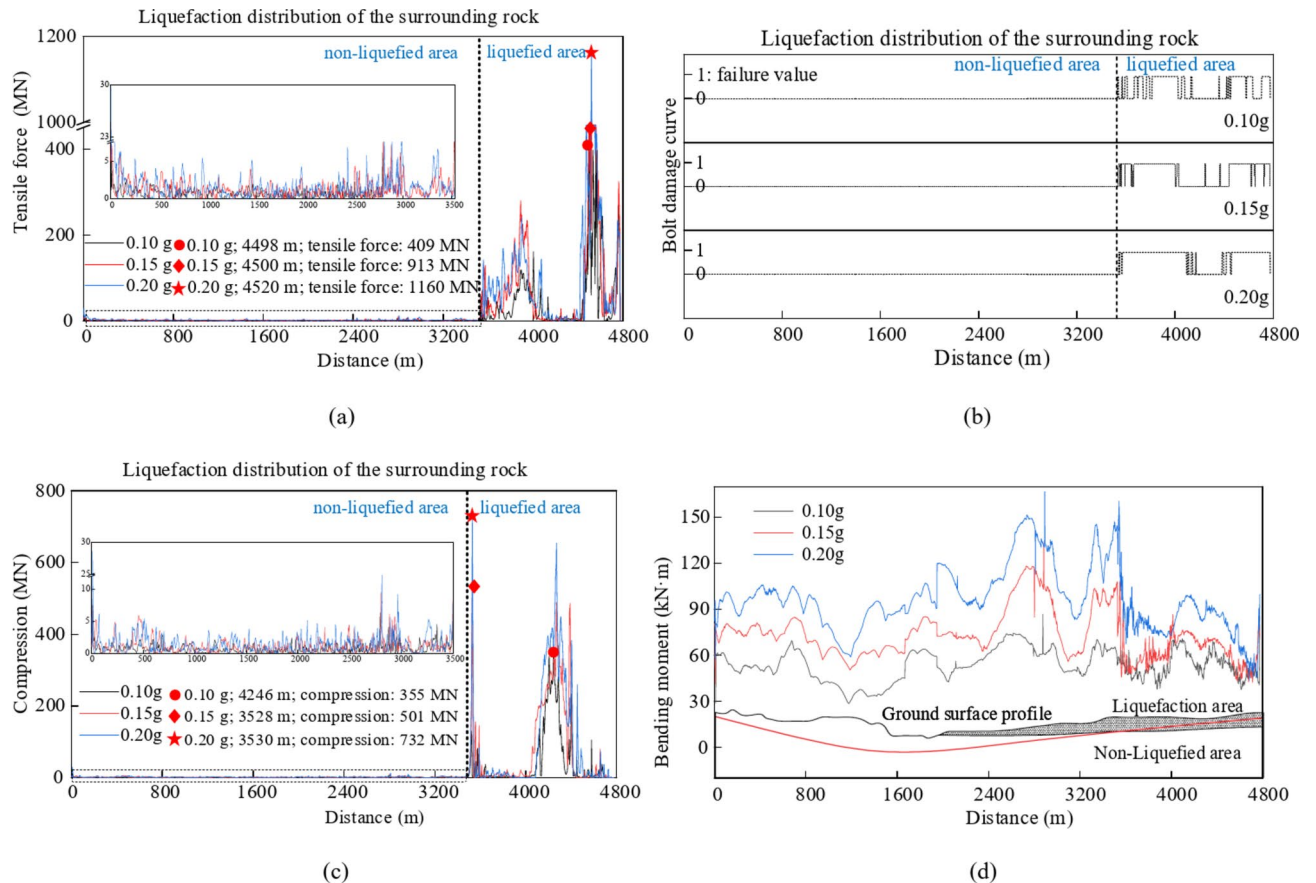


Fig. 18. Inner force responses of shield tunnel. (a) Tensile force response; (b) Bolt damage distribution; (c) Compression response; (d) Bending moment response.

To clearly represent the tunnel longitudinal bolt damage distribution, the bolt damage distribution diagram is drawn in Fig. 18 (b). When the tensile force exceeds 27.6 MN, the bolt damage value is defined as 1 while the reverse is defined as 0. The bolt damage zone is mainly distributed in the liquefied slippage area. With the increase of PBA, the bolt damage zone is more continuous and extensive. Furthermore, the bolt damage area is significantly wider than the opening damage curve. Therefore, the bolt damage should be more concerned for shield tunnels crossing liquefied slippage areas.

Figure 18 (c) shows that the overall variation pattern of the axial compression curve in the central section of the shield tunnel ring intersegment has some similarities with the opening width curve. With the increase of PBA, the amplitude change of axial compression in the non-liquefaction zone is small, but the liquefaction slippage zone increases sharply. The maximum pressure position under 0.10 g working condition is located at the valley bottom between B7 and B8, which is different from the maximum position of 0.20 g and 0.30 g. The reason for the above phenomenon may be that the soil layer on both sides is liquefied and then squeezed towards the valley bottom, thus causing the ring intersegment to produce greater compression. The peak compression position of the shield tunnel ring intersegment section is not the same as the tensile peak position, and the peaks' locations appear alternately.

Figure 18 (d) shows the curve of the bending moment in the central section of the shield tunnel ring intersegment under different ground motion intensities. The curve patterns of bending moments under different ground motion intensities are similar. The bending moment has a tendency to increase at the bottom of the multi-stage slope. When the tunnel crosses the non-liquefied soil layer, the bending moment curve is relatively smooth. When the tunnel crosses the liquefied soil layer, the bending moment curve shows an oscillation phenomenon. It illustrates that the lateral slippage of the liquefied soil layer will aggravate the complexity of the longitudinal deformation. The increase amplitude of the bending moment in the non-liquefaction zone is approximately proportional to the increase of PBA. The difference of tunnel bending moment under different PBA in the liquefaction zone is small.

The above research results indicate that the liquefied slippage of the site will aggravate the inner force. The shield tunnel is subjected to large compression, tensile force and more severe deformation, which causes the shield tunnel to produce serious local damage. Therefore, when the shield tunnel crosses a site with high soil liquefaction grade and a certain slope, it is necessary to carry out foundation treatment of the site according to 'Seismic Design Standard for Underground Structures (GB/T51336-2018).

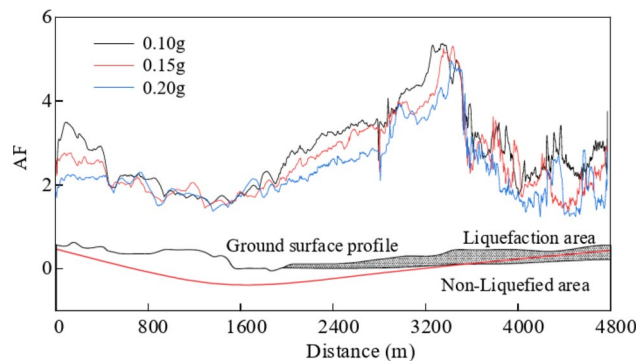


Fig. 19. AF peak values along the tunnel longitudinal direction.

Longitudinal peak acceleration of tunnel

It can be seen from Fig. 19 that the variation pattern of the longitudinal ring intersegment acceleration amplification factors of the tunnel has some similarities with the topography of the site. The AF decreases with the increase of PBA, but the overall change is small. The above phenomenon indicates that the longitudinal AF crossing the site is mainly influenced by the topography. Meanwhile, the oscillation of the peak acceleration amplification factor curve between adjacent ring intersegment of tunnels crossing the liquefied slippage zone is more obvious. The above conclusions show that the difference of acceleration amplification factors of adjacent ring intersegments is large, which further indicates that the lateral slippage will aggravate the longitudinal seismic response of the shield tunnel.

Conclusions

A refined beam-spring model passing through the liquefaction slip zone based on the generalized response displacement method was established, and the feasibility of the method was analyzed. Based on the actual project of the shield tunnel across the lower reaches of the Yangtze River entrance to the sea, the effect of the site liquefaction slippage on the longitudinal seismic response of the shield tunnel was investigated. The following conclusions were reached:

- (1) The generalized response displacement method can simulate the effects of site liquefaction, topographic effects and slippage on the seismic response of shield tunnels. It is feasible to use the generalized response displacement method to investigate the longitudinal seismic response of shield tunnels in liquefied slippage areas.
- (2) Liquefied slippage under an earthquake will lead to a larger opening width at the ring intersegment, section tensile force and compression of the shield tunnel, which will easily cause serious seismic damage such as bolt failure and water leakage.
- (3) In terms of the opening width, the liquefaction of the site will not cause serious damage to the tunnel structure. Slippage is the main reason to cause structural damage.
- (4) The axial compression and tensile force curves of the longitudinal ring intersegment section of the tunnel are consistent with the opening curve. The bending moment maximum curve and the acceleration amplification factor curve have some similarity with the topographic relief of the site, and the curves located in the liquefied layer all show obvious oscillation phenomena.

The generalized response displacement method has some limitations. The foundation spring stiffness is set to a constant value, which is inconsistent with the constant change of soil stiffness around the tunnel during an actual earthquake. In addition, the typical seismic damages (segment concrete damage and circumferential dislocation), refined modelling of tunnel internal structure and elliptical deformation of structural section cannot be considered.

Data availability

The datasets used and/or analyzed during the current study are available from the corresponding author on reasonable request.

Received: 9 February 2025; Accepted: 19 March 2025

Published online: 18 April 2025

References

1. Zhao, K. et al. Seismic response of immersed tunnel in liquefiable seabed considering ocean environmental loads. *Tunn. Undergr. Space Technol.* **115**, 104066 (2021).
2. Pan, H. S., Tong, L. Y., Wang, Z. S. & Yang, T. Effects of soil-cement mixing wall construction on adjacent shield tunnel linings in soft soil. *Arab. J. Sci. Eng.* **9**, 06705 (2022).
3. Zhuang, H. Y., Wang, R., Chen, G. X., Miao, Y. & Zhao, K. Shear modulus reduction of saturated sand under large liquefaction-induced deformation in cyclic torsional shear tests. *Eng. Geol.* **240**, 110–122 (2018).

4. Shen, Y. et al. Seismic response of shield tunnel structure embedded in soil deposit with liquefiable interlayer. *Comput. Geotech.* **152**, 105015 (2022).
5. Nokande, S., Jafarian, Y. & Haddad, A. Shaking table tests on the liquefaction-induced uplift displacement of circular tunnel structure. *Undergr. Space*. **10**, 182–198 (2023).
6. Liang, J. W. et al. Shaking table test and numerical simulation on ultra-large diameter shield tunnel passing through soft-hard stratum. *Soil Dyn. Earthq. Eng.* **147**, 106790 (2021).
7. Liu, J. B., Wang, D. Y. & Bao, X. Longitudinal integral response deformation method for the seismic analysis of a tunnel structure. *Earthq. Eng. Eng. Vib.* **20**(4), 887–904 (2021).
8. Kawamata, Y., Nakayama, M., Towhata, I. & Yasuda, S. Dynamic behaviors of underground structures in E-Defense shaking experiments. *Soil Dyn. Earthq. Eng.* **82**, 24–39 (2021).
9. Yu, H. T. et al. Multi-point shaking table test of a long tunnel subjected to non-uniform seismic loadings. *Bull. Earthq. Eng.* **16**(2), 1041–1059 (2018).
10. Dowding, C. H. & Rozen, A. Damage to rock tunnels from earthquake shaking. *J. Geotech. Eng. Div.* **104**(2), 175–191 (1978).
11. Sharma, S. & Judd, W. R. Underground opening damage from earthquakes. *Eng. Geol.* **30**, 263–276 (1991).
12. Yu, H. T., Chen, J. T., Bobet, A. & Yuan, Y. Damage observation and assessment of the Longxi tunnel during the Wenchuan earthquake. *Tunn. Undergr. Space Technol.* **54**, 102–116 (2016).
13. Yu, H. T., Yuan, Y. & Bobet, A. Seismic analysis of long tunnels: A review of simplified and unified methods. *Undergr. Space*. **2**(02), 73–87 (2017).
14. Okamoto, S. & Tamura, C. Behaviors of subaqueous tunnels during earthquakes. *Earthq. Eng. Struct. Dyn.* **1**(3), 253–266 (1972).
15. Tsinidis, G., Pitilakis, K., Madabhushi, G. & Heron, C. Dynamic response of flexible square tunnels: Centrifuge testing and validation of existing design methodologies. *Geotechnique* **65**(05), 401–417 (2015).
16. Chen, R. R., Taiebat, M., Wang, R. & Zhang, J. M. Effects of layered liquefiable deposits on the seismic response of an underground structure. *Soil Dyn. Earthq. Eng.* **113**, 124–135 (2018).
17. Davoodi, M., Senent, S., Keshavarz, A. & Jimenez, R. Three-dimensional seismic face stability of shield tunnels in undrained clay. *Undergr. Space* **15**, 26–43 (2024).
18. Hashash, Y. M. A., Hook, J. J., Schmidt, B. & Yao, J. I. C. Seismic design and analysis of underground structures. *Tunn. Undergr. Space Technol.* **16**(4), 247–293 (2001).
19. Xu, Z. G., Du, X. L., Xu, C. S., Jiang, J. W. & Han, R. B. Simplified equivalent static methods for seismic analysis of shallow buried rectangular underground structures. *Soil Dyn. Earthq. Eng.* **121**, 1–11 (2019).
20. Wang, W. et al. A solution of subgrade modulus for response displacement method of circular underground structures. *Shock Vib.* **2021**, 3654147 (2021).
21. Miao, Y., Yao, R. L., Ruan, B. & Zhuang, H. Y. Seismic response of shield tunnel subjected to spatially varying earthquake ground motions. *Tunn. Undergr. Space Technol.* **77**, 216–226 (2018).
22. Miao, Y. et al. Improved Hilbert spectral representation method and its application to seismic analysis of shield tunnel subjected to spatially correlated ground motions. *Soil Dyn. Earthq. Eng.* **111**, 119–130 (2018).
23. Chen, G. X. et al. Nonlinear response characteristics of undersea shield tunnel subjected to strong earthquake motions. *J. Earthq. Eng.* **24**(03), 351–380 (2020).
24. Zhang, J. S., Zhang, S. S., Zhou, G. M., Xu, X. & Feng, J. M. Collapse mechanism of gentle inclined and fine-grained soil slope on reservoir bank. *J. Eng. Geol.* **24**(05), 752–759 (2016) (in Chinese).
25. Chen, G. X., Liu, X. Z. & Zhan, J. Y. Undrained dynamical behavior of Nanjing flake-shaped fine sand under cyclic loading. *J. Central South Univ. Technol.* **15**(2), 215–221 (2008).
26. Zhuang, H. Y. & Chen, G. X. A viscous-plastic model for soft soil under cyclic loadings. *Proc. Geo-Shanghai Conf.* **150**, 343–350 (2006).
27. Zhuang, H. Y. et al. Liquefaction-induced lateral spreading characteristics of the fluvial terraces at the lower reaches of Yangtze River. *Eng. Geol.* **346**, 107900 (2025).
28. Ben-Zeev, S., Goren, L., Toussaint, R. & Aharonov, E. Drainage explains soil liquefaction beyond the earthquake near-field. *Nat. Commun.* **14**(1), 5791 (2024).
29. Ni, X. Q., Zhang, Z., Ye, B. & Zhang, S. Unique relation between pore water pressure generated at the first loading cycle and liquefaction resistance. *Eng. Geol.* **296**, 106476 (2022).
30. Zhuang, H. Y., Hu, Z. H., Wang, X. J. & Chen, G. X. Seismic responses of a large underground structure in liquefied soils by FEM numerical modelling. *Bull. Earthq. Eng.* **13**(12), 3645–3668 (2015).
31. Zhuang, H. Y., Wu, X. Z. & Chen, G. X. Study of nonlinear static and dynamic coupling interaction of soil-underground structure considering initial static stress. *Chin. J. Rock Mech. Eng.* **30**(1), 3112–3119 (2011) (in Chinese).
32. Chen, S. et al. Experimental investigation of the seismic response of shallow-buried subway station in liquefied soil. *Soil Dyn. Earthq. Eng.* **136**, 106153 (2020).
33. Xie, J. N., Li, P. F., Zhang, M. J., Jia, F. & Li, S. H. Analytical solutions of ground settlement induced by yaw in a space curved shield tunnel. *Undergr. Space*. **13**, 86–103 (2023).
34. Chen, R. P., Tang, L. J., Liang, D. S. & Chen, Y. M. Face stability analysis of shallow shield tunnels in dry sandy ground using the discrete element method. *Comput. Geotech.* **38**(2), 187–195 (2011).
35. Klar, A. & Klein, B. Energy-based volume loss prediction for tunnel face advancement in clays. *Geotechnique* **64**(10), 776–786 (2014).
36. Chen, G. X. & Liu, X. Z. Testing study on ratio of dynamic shear moduli and ratio of damping for recently deposited soils in Nanjing and its neighboring areas. *Chin. J. Rock Mech. Eng.* **23**(08), 1403–1410 (2004) (in Chinese).
37. Xu, C. S., Pan, X., Feng, C. Q., Du, X. L. & Xu, J. L. Experimental research on dynamic shear characteristics of liquefaction circulating flow soil. *China Civ. Eng. J.* **53**(03), 95–102 (2020) (in Chinese).
38. Yang, J., Zhuang, H. Y., Wang, W., Zhou, Z. H. & Chen, G. X. Seismic performance and effective isolation of a large multilayered underground subway station. *Soil Dyn. Earthq. Eng.* **142**, 106560 (2021).
39. Tso, W., Zhu, T. & Heidebrecht, A. Engineering implication of ground motion A/V ratio. *Soil Dyn. Earthq. Eng.* **11**(3), 133–144 (1992).
40. Yu, H. T., Chen, J. T., Yuan, Y. & Zhao, X. Seismic damage of mountain tunnels during the 5-12 Wenchuan earthquake. *J. Mount. Sci.* **13**(11), 1958–1972 (2016).
41. Huo, H., Bobet, A., Fernández, G. & Ramírez, J. Load transfer mechanisms between underground structure and surround ground: Evaluation of the failure of the Daikai station. *J. Geotech. Geoenviron. Eng.* **131**(12), 1522–1533 (2005).
42. Zhuang, H. Y., Cheng, S. G. & Chen, G. X. Numerical simulation and analysis of earthquake damages of Dakai metro station caused by Kobe earthquake. *Rock Soil Mech.* **29**(1), 245–250 (2008) (in Chinese).
43. Sun, L. T., Lai, Z. C. & Bai, Y. Research on seismic wave delay and amplification methods in the shaking table test of large-span structures in mountain areas. *Appl. Sci.* **13**(11), 6728 (2023).
44. Yu, H. T. et al. Analytical solution for longitudinal seismic response of tunnel liners with sharp stiffness transition. *Tunn. Undergr. Space Technol.* **77**, 103–114 (2018).
45. Yuan, Y., Yang, Y. S., Zhang, S. H., Yu, H. T. & Sun, J. A benchmark 1 g shaking table test of shallow segmental mini-tunnel in sand. *Bull. Earthq. Eng.* **18**(11), 5383–5412 (2020).

46. Taboada-Urtazuastegui, V. M., Martinez-Ramirez, G. & Abdoun, T. Centrifuge modeling of seismic behavior of a slope in liquefiable soil. *Soil Dyn. Earthq. Eng.* **22**(9), 1043–1049 (2002).
47. He, B., Zhang, J. M., Li, W. & Wang, R. Numerical analysis of LEAP centrifuge tests on sloping liquefiable ground: Influence of dilatancy and post-liquefaction shear deformation. *Soil Dyn. Earthq. Eng.* **137**, 106288 (2020).
48. Spudich, P., Hellweg, M. & Lee, W. H. K. Directional topographic site response at Tarzana observed in aftershocks of the 1994 Northridge, California, earthquake: Implications for mainshock motions. *Bull. Seismol. Soc. Am.* **86**(1B), S193–S208 (1996).
49. Wang, H. Y. & Xie, L. L. Effects of topography on ground motion in the Xishan park Zigong city. *Chin. J. Geophys.* **53**(7), 1631–1638 (2010) (in Chinese).
50. Lee, K. M. & Ge, X. W. The equivalence of a jointed shield-driven tunnel lining to a continuous ring structure. *J. Can. Geotech. Eng.* **38**(3), 461 (2001).
51. Ye, F. et al. Model test study on effective ratio of segment transverse bending rigidity of shield tunnel. *Tunn. Undergr. Space Technol.* **41**, 193–205 (2014).

Acknowledgements

This study was financially supported by the National Natural Science Foundation of China (51978333, 52278354, 52378347 and 51908237), and the Fundamental Research Funds for the Central Universities (2020kfyXJJS114). The authors wish to gratefully acknowledge these supports.

Author contributions

Xiaoxiong Li: Validation, Formal analysis, Visualization, Software, Writing—original draft. Haiyang Zhuang: Validation, Formal analysis, Visualization, Software, Writing—review & editing. Bin Ruan: Conceptualization, Methodology, Software, Investigation, Writing—original draft. Kai Zhao: Resources, Writing—original draft. Guoxing Chen: Writing—review & editing, Supervision.

Funding

The National Natural Science Foundation of China, 51978333, 52278354, 52378347, the Fundamental Research Funds for the Central Universities, 2020kfyXJJS114.

Declaration

Competing interests

The authors declare no competing interests.

Additional information

Correspondence and requests for materials should be addressed to X.L. or K.Z.

Reprints and permissions information is available at www.nature.com/reprints.

Publisher's note Springer Nature remains neutral with regard to jurisdictional claims in published maps and institutional affiliations.

Open Access This article is licensed under a Creative Commons Attribution-NonCommercial-NoDerivatives 4.0 International License, which permits any non-commercial use, sharing, distribution and reproduction in any medium or format, as long as you give appropriate credit to the original author(s) and the source, provide a link to the Creative Commons licence, and indicate if you modified the licensed material. You do not have permission under this licence to share adapted material derived from this article or parts of it. The images or other third party material in this article are included in the article's Creative Commons licence, unless indicated otherwise in a credit line to the material. If material is not included in the article's Creative Commons licence and your intended use is not permitted by statutory regulation or exceeds the permitted use, you will need to obtain permission directly from the copyright holder. To view a copy of this licence, visit <http://creativecommons.org/licenses/by-nc-nd/4.0/>.

© The Author(s) 2025